Title

3D Numerical Analyses of Column-Supported Embankments: Failure Heights, Failure Modes, and Deformations

Journal

Journal of Geotechnical and Geoenvironmental Engineering, 146(12)

ISSN

1090-0241

Authors

Huang, Zhanyu
Ziotopoulou, Katerina
Filz, George M

Publication Date

2020-12-01

DOI

10.1061/(asce)gt.1943-5606.0002385

Peer reviewed

3D Numerical Analyses of Column-Supported Embankments: Failure Heights, Failure Modes, and Deformations

Zhanyu Huang, A.M.ASCE[1]; Katerina Ziotopoulou, A.M.ASCE[2]; and George M. Filz, Dist.M.ASCE[3]

Abstract: Design of column-supported embankments (CSE) requires the evaluation of global stability using the conventional limit equilibrium method (LEM). Yet, for CSEs using unreinforced concrete columns and load transferring geogrids, the failure mechanisms and corresponding soil-structure interactions are not well understood. There is increasing evidence pointing to large bending moments in columns and failure of columns in flexure, as opposed to a failure by shear as assumed in limit equilibrium analyses. In response to these design uncertainties, the failure height, failure mode, and deformations of eight column-supported embankment scenarios were investigated using three-dimensional (3D) numerical analyses. For the same embankment scenarios at failure height, factors of safety (FS) were then calculated using the two-dimensional (2D) LEM for investigating its applicability in evaluating global stability of CSEs. The 3D numerical analyses examined CSE stability for the limiting conditions at undrained end-of-construction and after long-term dissipation of excess pore water pressures. The numerical model included representations of flexural tensile failure in the concrete columns and tensile failure in the geosynthetic reinforcement. Scenarios consisted of a base case with typical concrete column design, five single-parameter variations using base case conditions, and two multiparameter variations using base case conditions. The undrained condition was the most critical, and two failure modes were found: (1) multisurface shearing in the embankment coupled with bending failure of columns and near-circular shear failure in the clay, and (2) multisurface shearing in the embankment coupled with bending failure of columns and shearing in the upper portion of the soft foundation clay. Both failure modes were accompanied by a rupture of the geosynthetic when included in the load transfer platform. Soil-column interactions were complex, and many columns failed in bending at lower embankment heights than those that produced collapse. The factors of safety calculated using the LEM were overstated. This is because the LEM assumes failure by shear, which has limited applicability for examining the complex mechanisms by which CSEs fail. The practical implication is that the LEM should not be used for evaluating global stability of this system type and, by extension, other system types in which soil-structure interactions result in failures controlled by mechanisms other than shear. **DOI: 10.1061/(ASCE)GT.1943-5606.0002385.**

Introduction

Column-supported embankments (CSEs) have been used more frequently in recent decades for construction on soft soils. With appropriate design, CSEs can enable accelerated construction and high performance through the transfer of embankment and service loads to a competent stratum at depth via stiff foundation columns. Often, a load transfer platform (LTP) is constructed at the embankment base, and it consists of quality coarse-grained fill reinforced with one or more layers of geosynthetic. The load transfer mechanism occurs by the simultaneous soil arching in the embankment, differential settlement in the foundation, frictional resistance on the column shafts, and membrane action in the geosynthetic.

Design of CSEs requires evaluation of stability, as is necessary for all embankments. In the recommendations by Schaefer et al. (2017) for CSE design in the US, and with reference to the British standard (BSI 2010), consideration must be given to the ultimate limit states of embankment lateral sliding and global instability. Embankment lateral sliding is assumed to occur by the embankment mass sliding over the foundation with the concurrent mobilization of an active condition in the embankment. Geosynthetic reinforcement is recommended if the embankment active-thrust cannot be resisted by the foundation undrained shear strength (s_u) mobilized over the slope length by a safety factor of 1.5. Global instability is assumed to occur by shear failure through the embankment and column foundation. The conventional limit equilibrium method (LEM) is recommended for evaluation of global instability, in which case, both the geosynthetic and columns are included in the analysis.

Fundamental to CSE stability evaluation is an understanding of all possible failure modes. However, there is currently a limited understanding of the failure modes that can occur in CSEs designed using unreinforced concrete columns and geosynthetics in the LTP. Investigations of CSE failure modes have been performed using centrifuge tests and numerical analyses, but these were predominantly for embankments supported by columns or elements installed using the deep mixing method (Adams 2011; Chai et al. 2017; Inagaki et al. 2012; Jamsawang et al. 2015; Kitazume and Maruyama 2007; Navin 2005; Shrestha et al. 2015; Yapage et al. 2013; Zhang et al. 2014), for which the column properties and design differ from unreinforced concrete columns. A fundamental

[1]Graduate Student Researcher, The Charles E. Via Jr. Dept. of Civil and Environmental Engineering, Virginia Tech, Blacksburg, VA 24061 (corresponding author). ORCID: https://orcid.org/0000-0002-3223-5272. Email: zhanyuh8@vt.edu

[2]Assistant Professor, Dept. of Civil and Environmental Engineering, Univ. of California, Davis, CA 95616. ORCID: https://orcid.org/0000-0001-5494-497X

[3]Professor, The Charles E. Via Jr. Dept. of Civil and Environmental Engineering, Virginia Tech, Blacksburg, VA 24061.

Note. This manuscript was submitted on October 10, 2019; approved on June 22, 2020; published online on October 7, 2020. Discussion period open until March 7, 2021; separate discussions must be submitted for individual papers. This paper is part of the ***Journal of Geotechnical and Geoenvironmental Engineering***, © ASCE, ISSN 1090-0241.

difference is that concrete columns are typically installed using isolated columns at low area replacement ratios (ARR) of 2.5%–10% (Collin, personal communication, 2018). Unreinforced concrete has low tensile strength, and such columns are more likely to fail in bending than in shear (King et al. 2018; Huang et al. 2019). Zhang et al. (2012) reported a CSE centrifuge model using columns consisting of cement, fly ash, and gravel, and this model failed under a combined mechanism of shearing through the soft soil, cracking of columns near the embankment toe, and failure of the material representing the geosynthetic. Questions remain regarding (1) the various possible CSE failure modes involving failure of both the concrete columns and geosynthetic reinforcement; (2) the design parameters that influence stability, including the specific geosynthetic contribution; and (3) whether and to what extent the conventional LEM is applicable for evaluating global stability of CSEs if failures involve soil-structure interactions and occur by mechanisms other than shear. This study was motivated by all three issues.

Scope of Study

This study consisted of three-dimensional (3D) numerical analyses of eight embankment scenarios constructed to failure, followed by equivalent two-dimensional (2D) limit equilibrium analyses in which factors of safety were calculated for the same embankments at failure height. The scope of the numerical analyses is provided subsequently, whereas the scope of the limit equilibrium analyses is provided in the "Results and Discussion" section. The limit equilibrium analyses were designed after discovery of the failure mechanisms using 3D numerical analyses and will be more easily understood once embankment failure mechanisms are discussed.

CSE failure modes were investigated using 3D finite-difference analyses in the commercial software FLAC3D version 5.01. This numerical platform has been utilized in past studies for analyzing lateral deformations in CSEs for different pore pressure conditions (Huang and Han 2009; Jenck et al. 2009; Mahdavi et al. 2016). Furthermore, it permits user implementation of an *undrained-dissipated* load path for examining the limiting conditions of lateral spreading in CSEs, as discussed in the section "Undrained-Dissipated Analyses." In an effort to make the analyses less computationally expensive, consideration was given to the (1) stability metric, (2) limiting conditions and corresponding numerical approach with regards to pore pressures, (3) material modeling, and (4) scenarios.

Both the embankment failure height and shear strength reduction factor (Griffiths and Lane 1999) were considered for the stability metric, but the failure height was selected based on a number of advantages. Not only is the failure height just as relatable to practice as the shear strength reduction factor, but also, the process of constructing an embankment to failure offers additional details with regard to the embankment performance during construction and up until failure. Constructing the embankments to failure also bypasses uncertainties introduced by reducing shear strengths in disproportion to other strength types, such as the flexural tensile strength of the concrete and the tensile capacity of the geosynthetic. Disproportionately reducing the shear strength could obscure the actual failure mechanism (e.g., flexural failure of columns) in favor of shear failure. Of course, an option was to simultaneously reduce all strength types, but the appropriate application of this approach requires a different investigation altogether. Thus, in comparison, it was more straight-forward to use the failure height as the stability metric.

The limiting conditions for analysis were undrained end-of-construction and long-term dissipated, as concluded on the basis of CSE case history data (Huang et al. 2019). The embankments were constructed in lifts in the undrained condition with excess pore water pressure development in the clay. This was followed by a dissipation of excess pore water pressures and consolidation. Equilibrium was computed for an undrained end-of-construction state and a long-term dissipated state at different embankment heights. The failure height was interpreted as the one at which equilibrium could not be established and at which deformations continually increased.

Columns and geosynthetic reinforcement were each assigned a failure criterion. Column zones were modeled using the Mohr-Coulomb failure criterion with a tensile cutoff. Orthotropic linear elastic geogrid elements (Itasca 2013b) were removed from the unit cell between columns in which the geogrid tensile strain exceeded 10%.

A total of eight scenarios were investigated, and comparisons were made for the failure height, failure mode, lateral toe displacement, and centerline surface settlement. The scenarios consisted of a base case and seven parametric variations using base case conditions (Table 1). The parameters for variation are important for CSE design and site characterization: the center-to-center column spacing (S_{col}), the column diameter (d_{col}), the geosynthetic stiffness (J), and the clay's undrained shear strength (s_u). Fig. 1 illustrates a schematic of the base case, whose geometry and site conditions

Table 1. Scenario parameters and ultimate limit state

	Parameters				Ultimate limit state		
Scenario	Center-to-center column spacing S_{col} (m)	Column diameter d_{col} (m)	Geosynthetic stiffness J (kN/m)	Undrained shear strength of clay s_u (kPa)	Embankment failure height H_{fail} (m)	Critical condition	Failure mode
Base case	2.4	0.46	438	4.8	6.1	Undrained	B: multisurface shearing in the embankment coupled with column bending failure and shearing in the top portion of the clay (Fig. 5).
1	3.0	—	—	—	5.5	Undrained	A: multisurface shearing in the embankment coupled with column bending failure and near-circular shear failure in the clay (Fig. 3).
2	—	0.36	—	—	6.4	Undrained	B
3	—	—	0 (no geogrid)	—	5.5	Undrained	B
4	3.0	0.36	0 (no geogrid)	—	4.0	Undrained	A
5	—	—	1459	—	8.5	Undrained	B
6	—	—	—	14.4	12.2	Undrained	B
7	—	—	1459	14.4	(>12.8)	N/A	The embankment was constructed to an upper bound height of 12.8 m without failing.

Note: Cells with em-dash (—) are assumed to contain the same value corresponding to the base case; and s_u is for the top of clay layer.

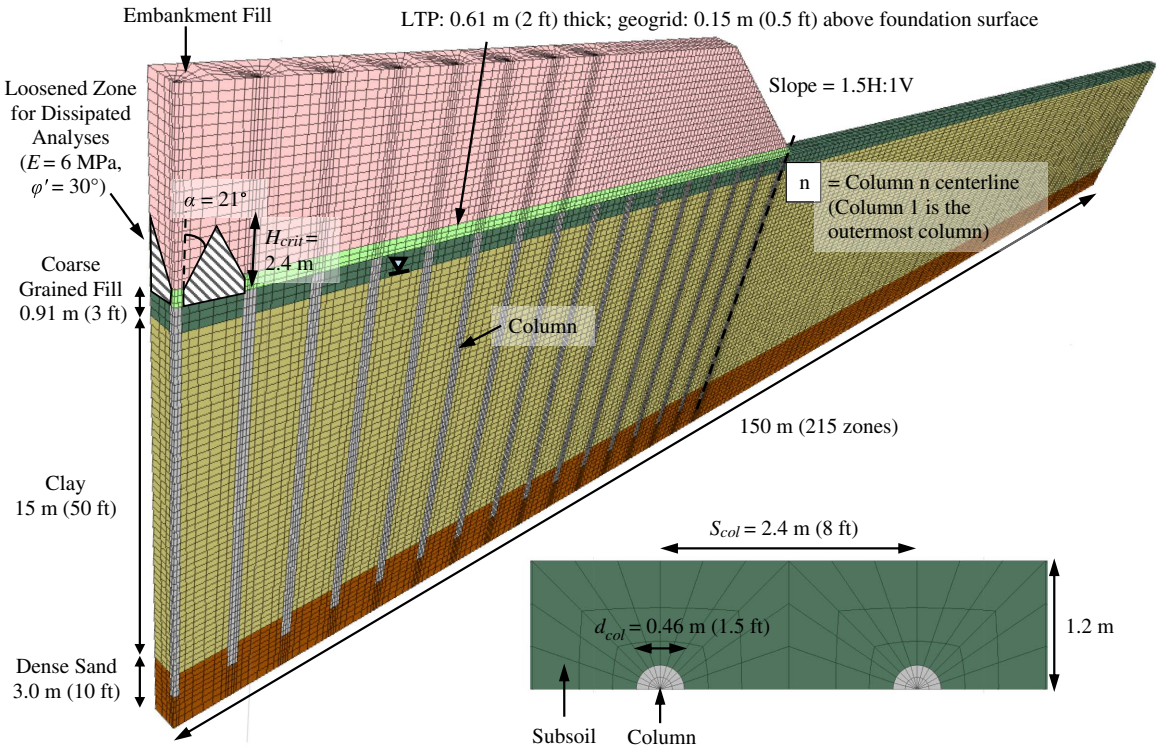

Fig. 1. Schematic of the base case CSE.

were selected to produce failure at an embankment height of about 6 m. The base case includes the following features:

- The columns had properties of unreinforced concrete, as produced during construction of vibro-concrete columns, and an area replacement ratio (ARR) of 2.8%. This ARR is in the lower range for typical CSE applications. Columns were installed in a square array, using S_{col} of 2.4 m (8 ft) and d_{col} of 0.46 m (1.5 ft) (Collin, personal communication, 2018).
- A layer of geosynthetic was included, using J of 438 kN/m (30,000 lb/ft) in both the longitudinal and transverse directions (Collin, personal communication, 2018).
- The clay was assigned properties corresponding to an s_u of 4.8 kPa (100 psf) at the layer top, and with s_u increasing with depth at a rate of 1.66 kPa/m (10.6 psf/ft), corresponding to a preconsolidation pressure profile that is at a constant increment above the vertical effective stress. This low s_u profile reflects the realistic and potentially challenging construction conditions for some CSEs (Zanzinger and Gartung 2002; Plomteux and Lacazedieu 2007).
- The clay was overlain by a layer of loose, coarse-grained fill, similar to what sometimes exists at CSE construction sites. The fill thickness was 0.91 m (3 ft).

The other scenarios were related to the base case as follows. The column spacing (S_{col}) was increased in Scenario 1, the column diameter (d_{col}) was decreased in Scenario 2, and no geosynthetic was used in Scenario 3. The three changes from the base case to create Scenarios 1–3 were applied simultaneously to produce Scenario 4. The geosynthetic stiffness (J) was increased in Scenario 5, and the undrained strength (s_u) of the clay was increased in Scenario 6. The two changes from the base case to create Scenarios 5 and 6 were applied simultaneously to produce Scenario 7. Thus, the base case and Scenarios 1–4 can be readily compared, as can the base case and Scenarios 5–7.

Scenarios 1, 2, and 4 have lower than typical ARRs, but they were adopted in the study based on the following considerations. In the interest of finding different failure mechanisms, using low ARRs allowed the embankments to be pushed to the limit. The use of low ARRs also expedited computations because failure can be reached at lower embankment heights. When combined, these reasons shaped the sensitivity analysis to investigate scenarios with typical and lower than typical ARRs.

Numerical Procedure

Numerical analyses were conducted using FLAC3D version 5.01 in large-strain mode. The following sections describe the rationale and procedure behind various aspects of the numerical model, including the undrained-dissipated approach for analyzing limiting conditions, the selection of constitutive models and material properties, the numerical domain and boundary conditions, and the loading sequence.

Undrained-Dissipated Analyses

The investigation of CSE failure modes in a computationally efficient manner required an analysis of limiting conditions rather than histories of deformations and pore pressures. The undrained-dissipated approach was selected for calculating an undrained end-of-construction state and a long-term state after dissipation of all excess pore water pressures. These are the two limiting conditions for lateral spreading analysis, as synthesized using CSE case history data (Huang et al. 2019). Field measurements show that vertical pressures in the foundation soil decrease with consolidation, indicating an ongoing development of soil arching at end-of-construction. This can be represented numerically as a limiting condition in which an undrained analysis of embankment construction

limits the subsoil consolidation and soil arching and produces the maximum increments of vertical and lateral earth pressure in the foundation soil. Field measurements also show the increase in geosynthetic strain with the increase in vertical load transfer to columns and subsoil settlement. This can also be represented as a limiting condition in which a full dissipation of excess pore water pressures leads to consolidation and development of geosynthetic strains with the increase in vertical deflection. The long-term dissipated condition is of interest to failure analyses because a tensile failure of the geosynthetic could be accompanied by a reduction in the lateral restraint provided by the geosynthetic and an increase in loading on the foundation soil.

Previous works adopting the undrained-dissipated approach include a validation of the method (Huang et al. 2018), an example application of lateral spreading analysis of a CSE case history (Huang et al. 2019), and a parametric study investigating the effect of design parameters on lateral thrust distribution in CSEs (Huang 2019). First, the method of excess pore water pressure dissipation and computed consolidation deformations were validated using benchmark solutions (Huang et al. 2018). Benchmarks consisted of one-dimensional consolidation as well as consolidation with lateral drainage for which a fully coupled analysis was performed for comparison. The undrained-dissipated approach was then adopted for the analysis of a CSE case history using a 3D half-embankment domain (Huang et al. 2019). Material parameters were calibrated such that the system response at the undrained end-of-construction and long-term dissipated conditions agreed with instrumented case history data. Lastly, a 3D numerical parametric study totaling 140 scenarios was performed using the calibrated half-embankment model (Huang 2019). The CSE lateral thrust distribution was investigated at the two limiting conditions for all scenarios. Results from the parametric study indicate that the undrained-dissipated approach is appropriate for failure analyses of CSEs. Multiple scenarios with marginal conditions (i.e., very low column ARR) were found to approach global instability at undrained end-of-construction. Geosynthetic strains were found to maximize in the long-term dissipated condition for all scenarios. However, the aforementioned studies were limited by the adoption of purely elastic geogrid elements for which the influence of geosynthetic tensile failure on load path could not be examined. In addition, there was uncertainty regarding failure modes because a collapse was not initiated in any of the scenarios. The present study overcomes these limitations by adopting a failure criterion for the geosynthetic and by increasing the embankment height until embankment collapse occurred. Furthermore, failure is examined for a range of column ARRs.

The undrained-dissipated approach was implemented in the current study. The embankment was constructed in the undrained condition in which the foundation drainage was disabled, and an effective stress model was used to calculate excess pore water pressures in the clay. The embankment was constructed in lifts of 0.6 m (2 ft) up to a height of 3.0 m (10 ft) and then in lifts of 0.3 m (1 ft) to achieve heights above 3.0 m. For scenarios in which the embankment was expected to be very tall, 0.6 m lifts were used throughout construction. The model was solved for equilibrium and an undrained end-of-construction state after the construction of every lift. Following undrained loading, pore water pressures were returned to the hydrostatic condition, and the model was solved for consolidation and a long-term dissipated state. The first dissipated analysis was conducted at an embankment height (H_{emb}) of 3.0 m (10 ft), which is above the estimated critical height (H_{crit}) for differential settlement (McGuire 2011) based on the least conservative column arrangement used in the eight scenarios. Subsequent dissipated analyses were conducted for every 0.6-m (2-ft) or 1.2-m (4-ft) increase in the embankment height above $H_{emb} = 3.0$ m.

Calibrated values of Young's modulus (E) and effective friction angle (φ') were adopted in select embankment zones above the subsoil between columns in the long-term dissipated analyses (Fig. 1, shaded embankment regions). As observed in bench-scale and full-scale CSEs (McGuire 2011; Sloan 2011), fill in a limited region above the subsoil between columns became very loose during differential settlement due to shearing and a decrease in normal stresses. The geometry of the loosened zones was established using a correlation to the fill's φ', which was formulated using data from bench-scale CSEs for sands with a range of relative densities prior to differential settlement (McGuire 2011). The properties of the loosened zones were determined from the calibration of a 3D numerical embankment slice model using case history data for vertical load transfer and settlement at the subgrade level (Huang et al. 2019).

Soil Properties

Soil constitutive models and their input properties are listed in Table 2. All coarse-grained soils were represented as linear elastic and perfectly plastic with the Mohr-Coulomb failure criterion. The clay was modeled with Modified Cam Clay. An undrained shear strength (s_u) was selected for the clay at the layer top, and the corresponding preconsolidation pressure (p'_o) was determined using Eq. (1) (Wood 1990). The preconsolidation pressure profile was then selected to linearly increase with depth at a constant increment above the effective vertical stress

$$s_u = \frac{M}{2}\exp\left[\frac{(\Gamma - \upsilon_\lambda)}{\lambda} + \ln(p'_o) - \left(\frac{\kappa}{\lambda}\right)\ln\left(\frac{p'_o}{p'_i}\right)\right] \qquad (1)$$

Column Properties

Unreinforced concrete columns were modeled using the linear elastic and perfectly plastic Mohr-Coulomb failure criterion with a tensile cutoff. Properties were determined with reference to Fig. 2:

- The concrete was assumed to have an unconfined compressive strength (f'_c) of 17 MPa (2500 psi), which is typical for vibro-concrete columns (SHRP2 2012).

Table 2. Material properties of soils and columns

Material	γ (kN/m^3)	Model	φ' (degrees)	c' (MPa)	σ_t (MPa)	E (MPa)	ν	λ	κ	M	e_1
Embankment fill (sand)	18.9	MC	37, 30[a]	0	—	24, 6[a]	0.28	—	—	—	—
LTP (gravel)	21.2	MC	40, 30[a]	0	—	36, 6[a]	0.26	—	—	—	—
Foundation fill (sand)	18.1	MC	34	0	—	14	0.31	—	—	—	—
Clay	16.5	MCC	—	—	—	—	0.37	0.17	0.017	0.98	2.57
Bearing sand	22.8	MC	45	0	—	72	0.23	—	—	—	—
Concrete column	23.6	MC	43	3.7	1.6	21,500	0.20	—	—	—	—

Note: MC = Mohr-Coulomb; MCC = Modified Cam Clay; and e_1 is the void ratio at a reference pressure of 0.048 kPa (1 psf).
[a]Reduced material property values adopted for loosened zones in the dissipated analyses.

J. Geotech. Geoenviron. Eng., 2020, 146(12): 04020141

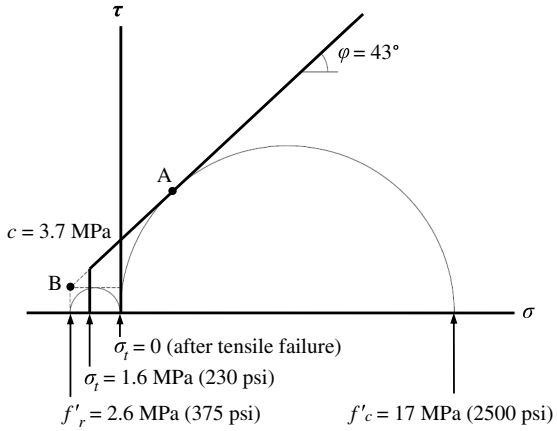

Fig. 2. Failure envelope of unreinforced concrete as adopted for columns.

- The flexural tensile strength (f_r') was 2.6 MPa (375 psi), estimated using Eq. (2) for normal weight concrete as a function of f_c' in US customary units (ACI 2011)

$$f_r' = 7.5\sqrt{f_c'} \tag{2}$$

- Points A and B were used in generating the portion of the failure envelope that defined the friction angle (φ) and the cohesion intercept (c). Point A is on the larger stress circle that represents the unconfined compression test (f_c'). Point B has a normal stress (σ) of f_r' and a shear stress (τ) that is half of f_r'. Point B was selected over a point on the smaller stress circle that represents the flexural tension test, so that a failure in tension would be calculated before a failure in shear. The resulting φ of 43° and c of 3.7 MPa are within range of reported values (Schädlich and Schweiger 2014; Pul et al. 2017).
- The tensile strength (σ_t) was assigned a reduced value of 1.6 MPa compared to f_r'. This was to account for the difference in the maximum tension calculated at zone centroids for a highly refined discretization of a single column and for a more practical discretization that could be incorporated in the half-embankment models. The isolated column with a highly refined discretization and $\sigma_t = f_r'$ was simply supported at the ends and subjected to a uniformly distributed line load. The magnitude of the line load was increased until flexural tensile failure occurred. Then, the same failure load was applied to an isolated column with the same practical zone discretization as used in the current study, and flexural failure occurred when σ_t was reduced to 1.6 MPa.
- A brittle behavior was modeled by reducing σ_t to zero after tensile failure.

Interface elements were applied at the column top, shaft, and base. Rough interfaces were assumed, using 0.98 and 0.95 for the ratio of interface friction angle to soil friction angle for coarse-grained soils and clay, respectively (Potyondy 1961). Interface normal and shear stiffnesses were assigned values equal to ten times the apparent stiffness of adjacent zones (Itasca 2013a).

Geosynthetic Properties

Properties of the geosynthetic reinforcement are listed in Table 3. Biaxial geogrids were modeled using orthotropic linear elastic structural geogrid elements of the constant strain triangle type (Itasca 2013b). The geogrid elements can sustain membrane stress but not bending, and they can develop tension under out-of-plane deformation when computed in the large-strain mode. Stiffnesses typical of biaxial geogrids were selected (Tensar International Corporation 2015; INOVA Geosynthetics 2017; Huesker 2019). The Poisson's ratio (ν) was 0 (Zhuang and Wang 2015). A small shear modulus (G) was assigned (Huang et al. 2019). There is uncertainty in the G of geosynthetics (Santacruz Reyes 2016), so a small value was selected to contrast between isotropic and orthotropic behavior. At the geogrid-soil interfaces, the friction angle was the same as the surrounding LTP (Cancelli et al. 1992; Cazzuffi et al. 1993; Liu et al. 2009), and the normal and shear stiffness values were 2×10^6 N/m (Eun et al. 2017; Liao et al. 2009).

Table 3. Material properties of geosynthetic reinforcement

Model	J (kN/m)	ν	G (kPa)
Orthotropic linear elastic	438, 1459	0	1

Note: J and ν apply to both longitudinal and transverse directions.

Failure of the geosynthetic reinforcement was manually implemented. When the transverse geosynthetic strain ($\varepsilon_{\text{trans}}$) in a unit cell reached 10%, tensile failure was assumed, and geogrid elements within the unit cell were removed. The $\varepsilon_{\text{trans}}$ was determined by summing the strain from the lateral spreading effect (ε_{lat}) and the strain from the vertical load transfer effect ($\varepsilon_{\text{vert}}$) [Eq. (3)]. The ε_{lat} value was calculated as the ratio of the change in the center-to-center column spacing (ΔS_{col}) in the transverse direction to the column clear span prior to deformation, which is the design S_{col} reduced by the edge length (a) of an equivalent square column cross-section [Eq. (4)]. This approach assumes that the geosynthetic did not slide appreciably at locations above the columns. The $\varepsilon_{\text{vert}}$ value was calculated according to the Parabolic method using the geosynthetic vertical deflection (d) [Eq. (5)]. The Parabolic method has been adopted in a number of design recommendations for calculating the geosynthetic strain under vertical deflection (Sloan et al. 2014; BSI 2016; Schaefer et al. 2017). The authors chose to estimate $\varepsilon_{\text{trans}}$ using established design methods rather than to rely on values automatically calculated in the geogrid elements because geosynthetic strains are highest above column edges (Ariyarathne et al. 2013; Han and Gabr 2002; Huang and Han 2009; Huang et al. 2019; Zhuang and Wang 2015), and the numerical calculation of this local strain effect is influenced by zone discretization (Huang et al. 2019)

$$\varepsilon_{\text{trans}} = \varepsilon_{lat} + \varepsilon_{\text{vert}} \tag{3}$$

$$\varepsilon_{lat} = \frac{\Delta S_{col}}{S_{col} - a} \tag{4}$$

$$\varepsilon_{\text{vert}} = \frac{8d^2}{3(S_{col} + \Delta S_{col} - a)^2} \tag{5}$$

Numerical Domain and Boundary Conditions

A 3D half-embankment slice geometry was adopted (Fig. 1), with the following numerical domain and boundary conditions. The centerline-to-toe width was kept constant at 37.5 m (123 ft) for all scenarios. The embankment was constructed at a slope of 1.5H:1V up to a maximum height of 12.8 m (42 ft), which was reported by Zhang et al. (2016) to be the tallest CSE ever constructed. The lateral extent was 4 times the centerline-to-toe width and 12 times the maximum embankment height (Huang et al. 2019). The centerline-to-shoulder width was selected to prevent the effects of the

centerline boundary on failure mechanisms near the slope. The column group did not extend beyond the embankment toe, but it did extend as close as possible to the embankment toe to avoid edge instability. Boundary conditions consisted of pins at the model base below the strong bearing layer, a free surface at the top, and rollers on all other external surfaces.

Loading Sequence

A loading sequence similar to the one described by Huang et al. (2019) was adopted in the current study, as follows:

1. In situ stresses were assigned to foundation soils and columns, which had the same density as the surrounding soils. Null material properties were assigned to zones in the LTP and embankment fill. Mechanical equilibrium was computed, and the resulting displacements were very small.
2. Column installation was simulated by gradually increasing column density while solving for mechanical equilibrium. The small displacements calculated thus far were zeroed.
3. The embankment was constructed in an undrained condition by disabling drainage and calculating excess pore water pressures in the submerged clay. The zone material model of the LTP and embankment fill was changed from null to Mohr-Coulomb. The embankment was constructed in the lift sizes as previously described, in which each lift was applied by gradually increasing the density while solving for equilibrium.
4. In the dissipated analysis, reduced material parameters (E and φ') representing loosened fill were applied to select embankment zones at the same time as excess pore water pressures were dissipated in one step. The model was solved for consolidation and mechanical equilibrium. The result was the long-term dissipated state.

Procedure for Limit Equilibrium Analyses

Using Slide version 8.031, 2D limit equilibrium slope stability analyses were performed to investigate the factors of safety for the embankment scenarios at failure height. The conventional limit equilibrium method is recommended for evaluating global stability of CSEs (Schaefer et al. 2017; BSI 2010). Analyses were performed in 2D, as is common in geotechnical practice. The limit equilibrium models had the following attributes:

- The same material properties as in the 3D numerical model were applied.
- The 2D models had the same embankment cross-sectional geometry as the 3D models, except for the columns. While columns were modeled as cylinders in 3D, they could only be modeled as rectangular areas in 2D, which would equate the columns to walls spanning the longitudinal direction of the embankment. To maintain equivalent shear strengths, the width of the walls in 2D was adjusted to achieve the same area replacement ratio as the columns in 3D. The resulting widths of the 2D walls were smaller than the original diameters of the 3D columns.
- FS were calculated using Spencer's method for 50 vertical slice divisions in each failure surface.

Results and Discussion

Results are provided for the embankment failure height, failure mode, and deformations. The discussion regarding failure heights and failure modes refers to the undrained calculation, as embankment stability was found to be most critical at undrained end-of-construction. Embankment deformations are discussed for both the undrained and dissipated conditions.

Embankment Failure Heights

Scenario failure heights (H_{fail}) are listed in Table 1. In this study, the effects of the different scenarios on the calculated H_{fail} are presented first and then followed by a discussion. The failure height was affected by all parameters investigated, as shown by comparing Scenarios 1–7 with the base case. Scenario 1, with a larger S_{col}, calculated a decrease in H_{fail} of 0.6 m. Scenario 2, with a smaller d_{col}, calculated a slight increase in H_{fail} of 0.3 m. Scenario 3, with the geogrid excluded, calculated a decrease in H_{fail} of 0.6 m. Scenario 4, which resulted from the simultaneous change in the three parameters that created Scenarios 1–3 from the base case, calculated a decrease in H_{fail} of 2.1 m. The H_{fail} for Scenario 4 was most influenced by S_{col} and geosynthetic tensile capacity, which is correlated to geosynthetic stiffness (J) because tensile rupture was assumed to occur at 10% strain. Scenario 5, with a greater geosynthetic J (and tensile capacity), calculated an increase in H_{fail} of 2.4 m. Scenario 6, with a greater s_u, calculated an increase in H_{fail} of 6.1 m. Scenario 7, which resulted from the simultaneous change in the two parameters that created Scenarios 5 and 6 from the base case, was constructed to a maximum height of 12.8 m without failing, and this was mostly due to the influence of the clay's s_u.

Scenario 2 calculated a slightly greater H_{fail} than the base case even though a smaller d_{col} was used. This is because embankment failure initiated after geosynthetic failure, which was defined by $\varepsilon_{\text{trans}}$ exceeding 10% in any unit cell between two columns, and the distribution of $\varepsilon_{\text{trans}}$ differed for Scenario 2 and the base case. At $H_{emb} = 6.1$ m, the base case failed after $\varepsilon_{\text{trans}}$ exceeded 10% in the unit cell between the 12th and 13th columns from the centerline. At the same height, Scenario 2 also calculated a large $\varepsilon_{\text{trans}}$ of 9.2% in the same unit cell, as well as a large $\varepsilon_{\text{trans}}$ in other unit cells, although none exceeded 10%. After the H_{emb} increased to 6.3 m, Scenario 2 failed following a geosynthetic rupture between the 11th and 12th columns from the centerline. Thus, the slight increase in H_{fail} in Scenario 2 relative to the base case was due to a slight change in the overall system response from the change in d_{col} and not because d_{col} had a significant influence on the failure height.

Failure Modes

Scenario failure modes are listed in Table 1. Two failure modes were observed for the undrained condition: (1) multisurface shearing in the embankment coupled with column bending failure and near-circular shear failure in the clay (Mode A), which occurred for Scenarios 1 and 4; and (2) multisurface shearing in the embankment coupled with column bending failure and sliding within the top portion of the clay (Mode B), which occurred for the base case and Scenarios 2, 3, 5, and 6. Other failure modes may be possible for CSE configurations outside the current scope of study. The sequences leading to failure are described in the following sections.

Multisurface Shearing in the Embankment Coupled with Column Bending Failure and Near-Circular Shear Failure in the Clay

This failure mode was found in Scenarios 1 and 4 in which the column ARRs are low (1.8% and 1.1%, respectively). Notable features for the failure mode include the following:

- Column bending failure that initiated in the outermost column and retrogressively developed toward inner columns. A retrogressive direction indicates a direction of growth uphill (Duncan et al. 2014).

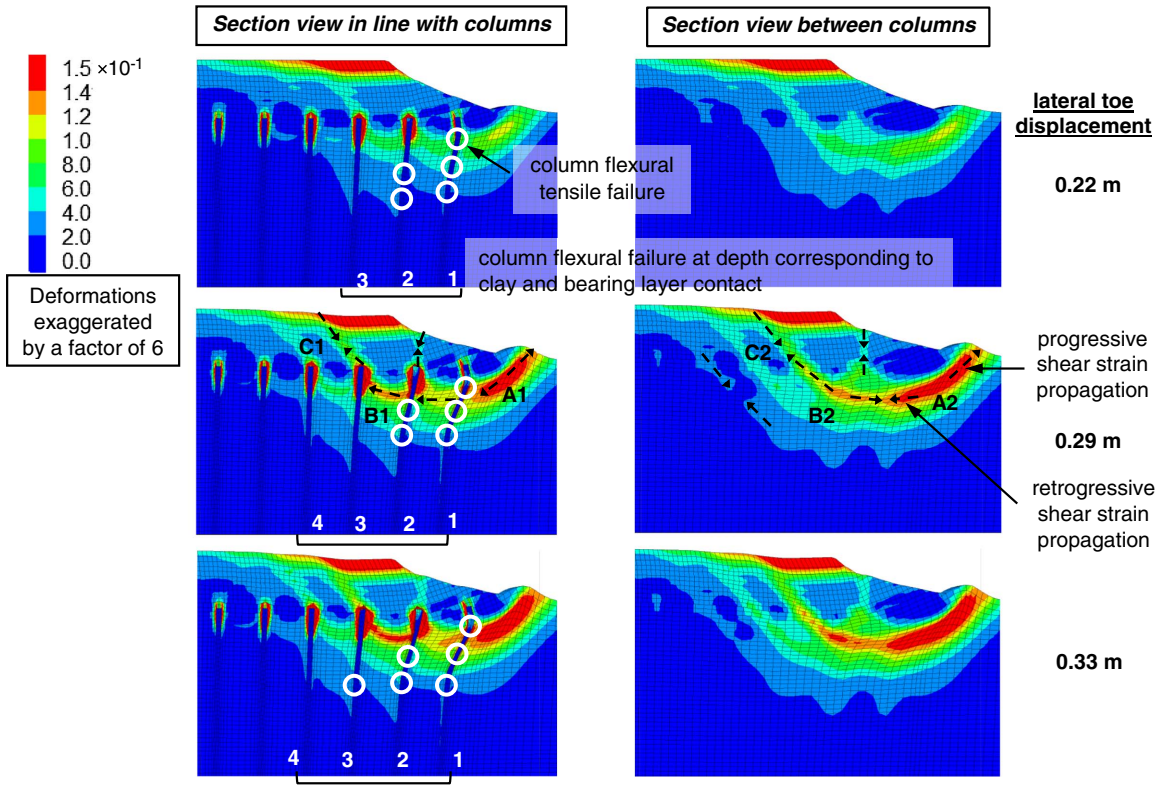

Fig. 3. Propagation of failure in Scenario 4 at $H_{fail} = 4.0$ m via shear strain contours and exaggerated deformations.

- Greater movement in clay than in columns near the embankment toe after column bending failure.
- Both progressive and retrogressive propagation of shear strains in the embankment and clay. A progressive direction indicates a direction of growth downhill (Duncan et al. 2014).
- Development of multiple shear bands in the embankment that converged to form a near-circular failure surface in the clay.
- Collapse following tensile failure of the geosynthetic, when geosynthetic was included in analysis (i.e., Scenario 1).

Fig. 3 illustrates the shear strain contours and exaggerated deformations for Scenario 4 at failure height and with increasing deformations. The number of shear bands in the embankment increased with displacement. The number of columns failing in flexural tension also increased. The columns were supporting axial compressive loads, but the bending moments were sufficient to produce tensile failure on the column cross-section. Shear strains developed both progressively and retrogressively, as annotated using arrows at locations A1 and A2, B1 and B2, and C1 and C2, which are corresponding locations in line and between columns, respectively.

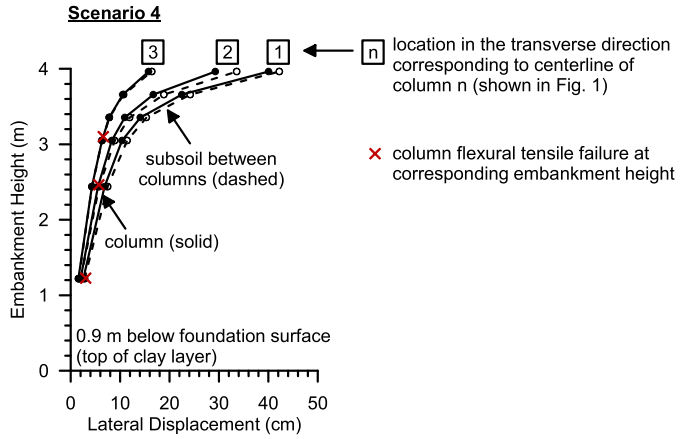

Fig. 4. Scenario 4 lateral displacements in columns and in subsoil between columns for embankment heights up to and including failure height.

Fig. 4 illustrates the lateral displacements of the columns and subsoil in between columns at an elevation corresponding to the top of the clay layer for Scenario 4. The lateral displacements in the three columns nearest to the embankment toe increased as the embankment height increased. The lateral displacements were largest for the column closest to the toe (labeled 1). At the same distance from the toe, the soil between the columns displaced more than the columns. Fig. 4 also shows the embankment height at which each column failed in tension due to column bending. The column closest to the embankment toe failed in flexural tension at an embankment height of 1.2 m, which is much less than the height of 4 m at which a collapse mechanism developed.

Multisurface Shearing in the Embankment Coupled with Column Bending Failure and Shearing in the Top Portion of the Clay

This failure mode was found in the base case and Scenarios 2, 3, 5, and 6. These scenarios have a column ARR of 2.8%, with the exception of Scenario 2, which has a low column ARR of 1.7%. Notable features common to all affected scenarios include the following:

- Extensive column bending failure that initiated in the outermost column and retrogressively developed toward inner columns.
- Greater lateral displacements in clay than in columns beneath the embankment slope, with the exception of the outermost

J. Geotech. Geoenviron. Eng., 2020, 146(12): 04020141

column, which experienced lateral displacements similar to the subsoil (i.e., the outermost column was pushed laterally along with the soil).
- Progressive and retrogressive propagation of shear strains in the embankment and clay.
- Development of multiple sets of complementary shear bands in the embankment.
- Development of high shear strains at the top of the clay layer.
- Collapse following tensile failure of the geosynthetic, when geosynthetic was included in analysis.

Fig. 5 illustrates shear strain contours and exaggerated deformations for the base case at increasing embankment heights up to the failure height of 6.1 m. The increase in embankment height resulted in the increasing development of high shear strain regions in the embankment involving multiple sets of complementary shear bands. The increase in embankment height also resulted in the increasing development of high shear strains at the top of the clay. When the embankment reached a height of 6.1 m, the geosynthetic failed in tension between Columns 4 and 5, and collapse was initiated. Column flexural tensile failure was calculated in the seven columns closest to the embankment toe, and the exaggerated deformations indicate column failure by bending.

Figs. 6(a–e) shows the lateral displacements of the columns and subsoil in between the columns at an elevation corresponding to the top of the clay layer. Lateral displacements were larger closer to the embankment toe (i.e., Location 1), and the relative movement of the subsoil and columns differed by location. The column closest to the embankment toe (labeled 1) had similar displacements as the subsoil, indicating it was pushed outwards along with the subsoil [Fig. 6(a)]. Columns 2, 3, and 4 displaced less compared to the subsoil [Figs. 6(b–d)]. Columns 1–4 were toward the toe from the location where the geosynthetic failed. Column 5 had similar lateral displacements as the subsoil [Fig. 6(e)], as was also the case for inner columns closer to the centerline.

Retrogressive failure of the columns occurred with the increase in embankment loading, as illustrated by the dash-dot lines in Figs. 6(a–d) for the base case. Columns 1 and 2 failed in flexural tension at an H_{emb} of 1.2 m (4 ft) and 3.0 m (10 ft), respectively. At $H_{emb} = 3.0$ m, the soil and column lateral movements were approximately the same. A further increase in the embankment height led to a greater movement in the clay than in the columns and flexural tensile failure of the inner columns. Columns 3 and 4 failed at $H_{emb} = 4.5$ and 4.9 m, respectively, when lateral displacements in the clay were already greater than in the columns [Figs. 6(c and d)]. By $H_{\text{fail}} = 6.1$ m, the seven columns closest to the embankment toe had failed in flexure, although the lateral movements in Columns 5–7 were about the same as in the subsoil. Column flexural tensile failure was also calculated at the elevation corresponding to the bottom of the clay and the top of the bearing layer. However, the column failure at depth was unlikely to have influenced the failure mechanism at the top of the clay layer and in the embankment.

Fig. 7 illustrates shear strain contours and exaggerated deformations for the base case at failure height with increasing displacements. The increase in displacements resulted in the development of additional shear bands in the embankment as well as an increase in the number of columns that failed in flexural tension due to bending. There were multiple regions in the embankment and foundation with high shear strains and for which shear strains propagated both progressively and retrogressively.

Deformations

The lateral displacement at the embankment toe for embankment heights up to but excluding failure is illustrated in Figs. 8(a and b)

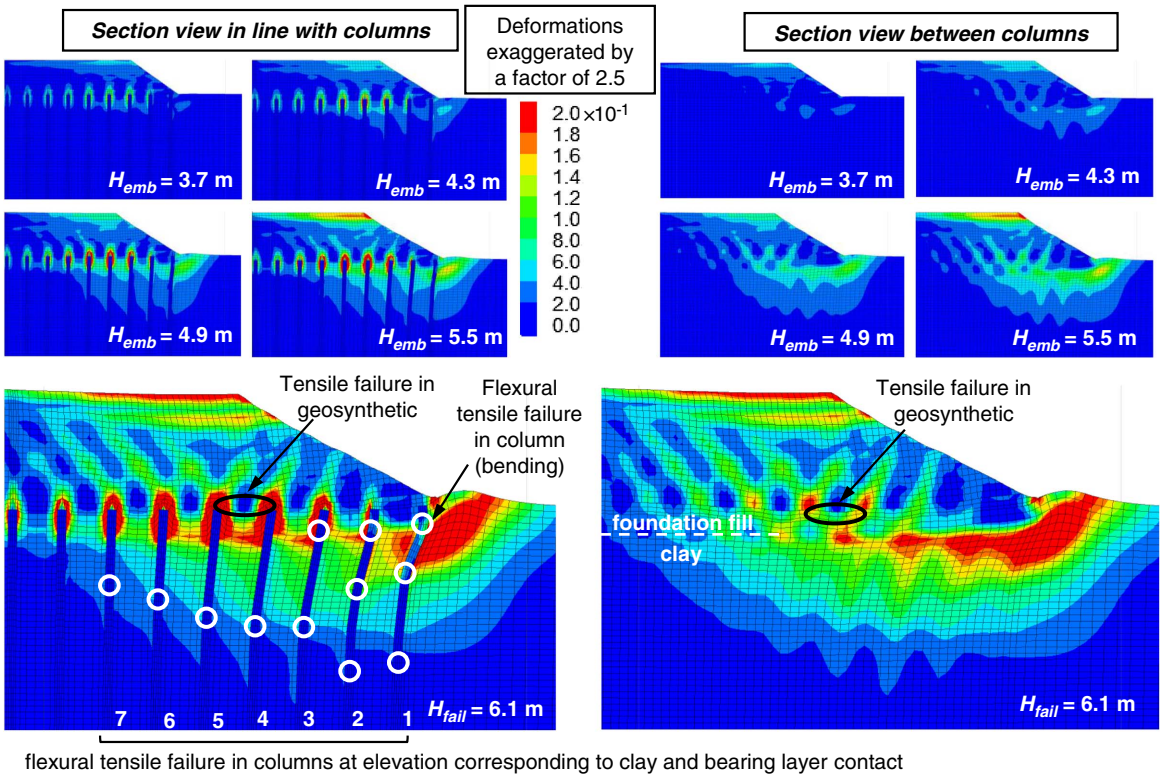

Fig. 5. Shear strain contours and exaggerated deformations for the base case at increasing embankment heights.

J. Geotech. Geoenviron. Eng., 2020, 146(12): 04020141

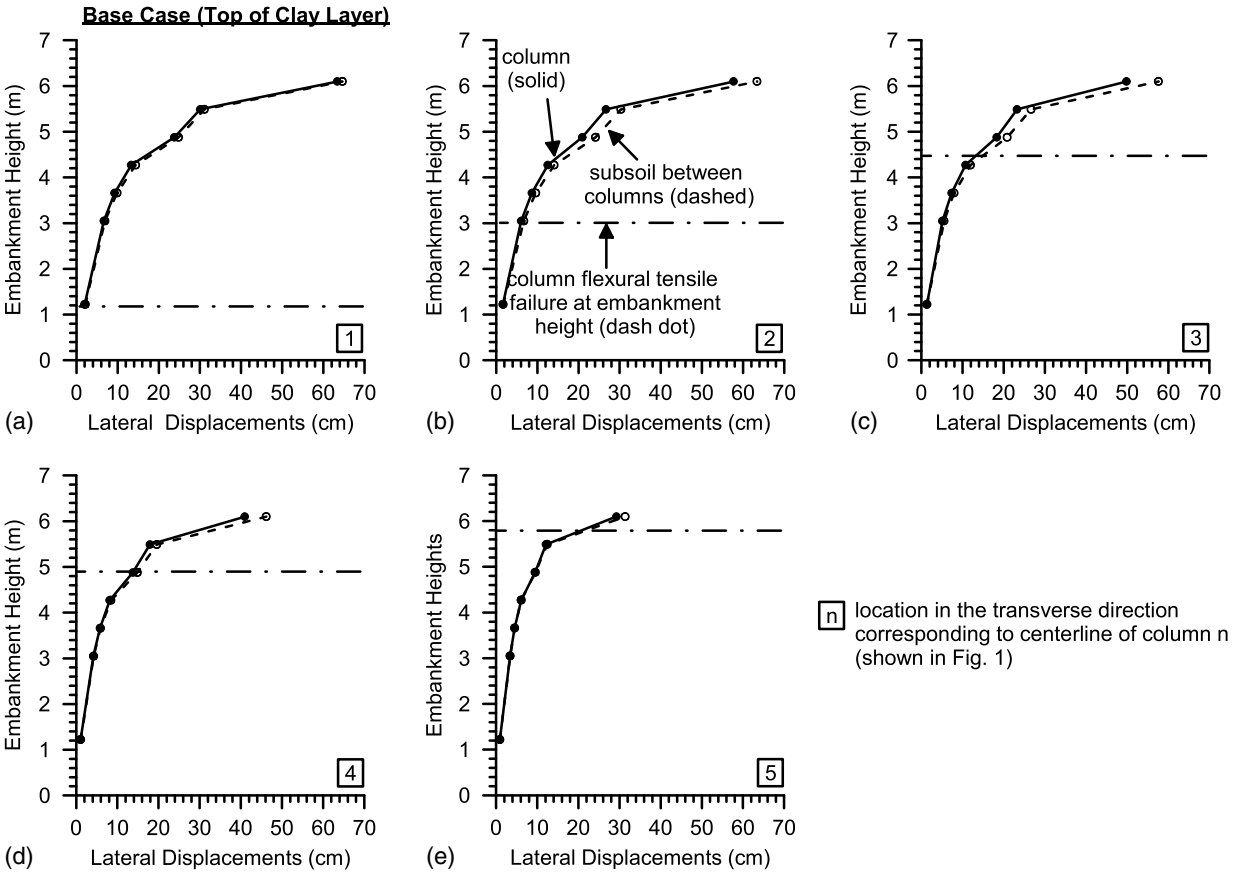

Fig. 6. Base case lateral displacements in columns and in subsoil between columns for embankment heights up to and including the failure height.

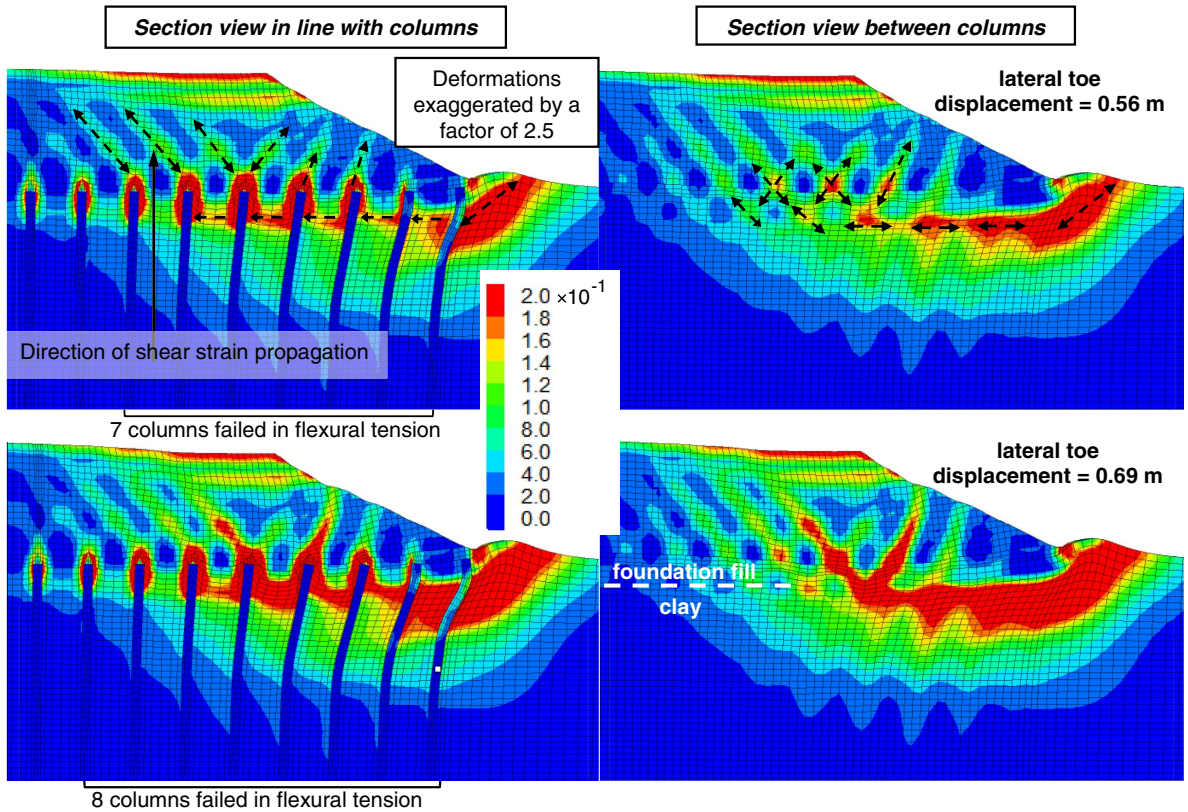

Fig. 7. Shear strain contours and exaggerated deformations for the base case at $H_{fail} = 6.1$ m showing the propagation of shear strains.

J. Geotech. Geoenviron. Eng., 2020, 146(12): 04020141

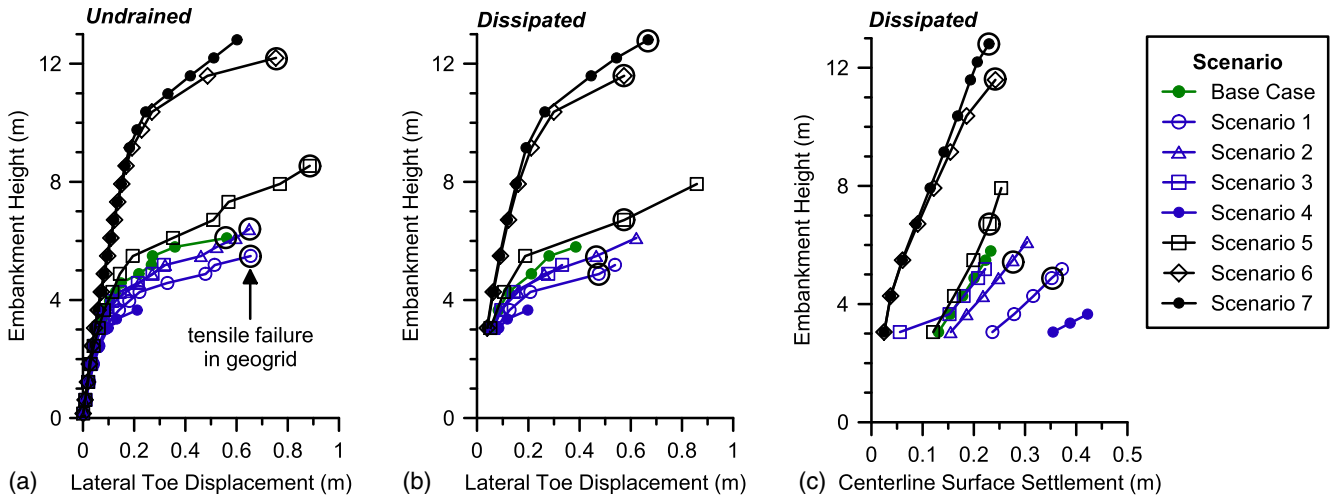

Fig. 8. Embankment height versus prefailure deformations in terms of (a) lateral toe displacement in the undrained condition; (b) lateral toe displacement in the dissipated condition; and (c) centerline surface settlement in the dissipated condition.

for the undrained and dissipated conditions, respectively. Lateral toe displacements were similar for the undrained and dissipated conditions, as was also reported by Huang et al. (2019). By including a geosynthetic with $J = 438$ kN/m, the lateral displacements decreased (the base case versus Scenario 3). By increasing the geosynthetic J from 438 to 1,459 kN/m, the lateral displacements also decreased (Scenario 5 versus the base case).

The total settlement at centerline for the long-term dissipated condition is illustrated in Fig. 8(c). Settlements that occur with excess pore water pressure dissipation impact serviceability, and thus, they are more important than settlements that occur in the undrained condition prior to consolidation. Fig. 8(c) illustrates that for Scenarios 1–3, in which each scenario represents a single-parameter change from the base case, the total settlement at any embankment height was influenced by the geosynthetic (Scenario 3), d_{col} (Scenario 2), and S_{col} (Scenario 1) in an increasing order of magnitude. Scenario 4, which represents a simultaneous change from the base case in all three parameters, calculated the largest total settlement primarily due to the influence of d_{col} and S_{col}. The influence of geosynthetic J and clay s_u on total settlements can be observed by comparing Scenarios 5 and 6 with the base case. The increase in s_u in Scenario 6 more effectively reduced settlements at any given embankment height. Scenario 7, which represents a simultaneous increase in s_u and J from the base case, calculated the smallest settlements largely due to the influence of s_u.

Figs. 8(a–c) show that the geosynthetic failed in tension in the dissipated condition for embankment heights below the failure height reached during undrained embankment placement. For example, Scenario 1 calculated geosynthetic tensile failure in the undrained condition at an embankment height (H_{emb}) of 5.5 m, and the embankment failed following geosynthetic rupture. During the dissipation of excess pore water pressures, the geosynthetic failed in tension starting at a H_{emb} of 4.9 m, but the embankment did not collapse. The long-term dissipated analysis was not performed with the embankment placed to 5.5 m because the embankment had already collapsed during undrained loading.

3D Numerical Analyses versus 2D Limit Equilibrium Analyses

For each embankment scenario, five 2D limit equilibrium analyses were conducted to investigate the extent to which the LEM is applicable for analyzing global stability of CSEs. The first analysis involved a search for the critical circular failure surface, which is a typical analysis for approximating the failure surface location and FS. The next four analyses involved calculating the FS for fully specified failure surfaces, whose geometries were user-defined and derived from 3D numerical computations (Fig. 9). Fig. 9(a) illustrates the multiple failure surfaces that develop during progressive failure as computed from 3D numerical analysis. Figs. 9(b–e) illustrate the corresponding 2D limit equilibrium analyses using fully specified failure surfaces: (1) Fig. 9(b) illustrates the slip surface that interacts with the geogrid and the minimum number of columns (N); (2) Fig. 9(c) illustrates the slip surface that interacts with the geogrid and the number of columns that is one greater than the minimum ($N + 1$); (3) Fig. 9(d) illustrates the smallest slip surface that interacts with the geogrid but not the columns, representing shear failure occurring in only the soils and not the columns; and (4) Fig. 9(e) illustrates the smallest slip surface that neither interacts with the geogrid nor the columns, representing a combination of Case (3) and the shear failure that occurs post geosynthetic failure.

Results from the 2D limit equilibrium analyses are discussed with reference to Table 4. Note that because the embankment scenarios were investigated at the failure height, the FS should be ≤1.0 for all scenarios. However, the LEM resulted in an FS greater than 1.0 for a number of analyses, as follows:

- The circular failure surface search yielded factors of safety larger than unity, and the FS corresponded to shallow slip surfaces within the embankment. These results indicate that a typical surface search using the LEM would not be able to find the critical failure surface, which, as determined from 3D numerical analyses, involves soil-structure interactions and failure within the foundation.
- The FS far exceeded unity when the slip surface was in interaction with the geogrid and columns. Slip surfaces interacting with N columns [Fig. 9(b)] and $N + 1$ columns [Fig. 9(c)] should both have an FS ≤ 1.0 because they were simultaneously developing at the failure height. However, the LEM calculated factors of safety that not only exceeded 1.0 but also increased with the number of columns in interaction with the slip surface. The increase in the FS is not only due to the increase in the slip surface length but also the increase in the shear resistance provided by a greater number of concrete columns in interaction

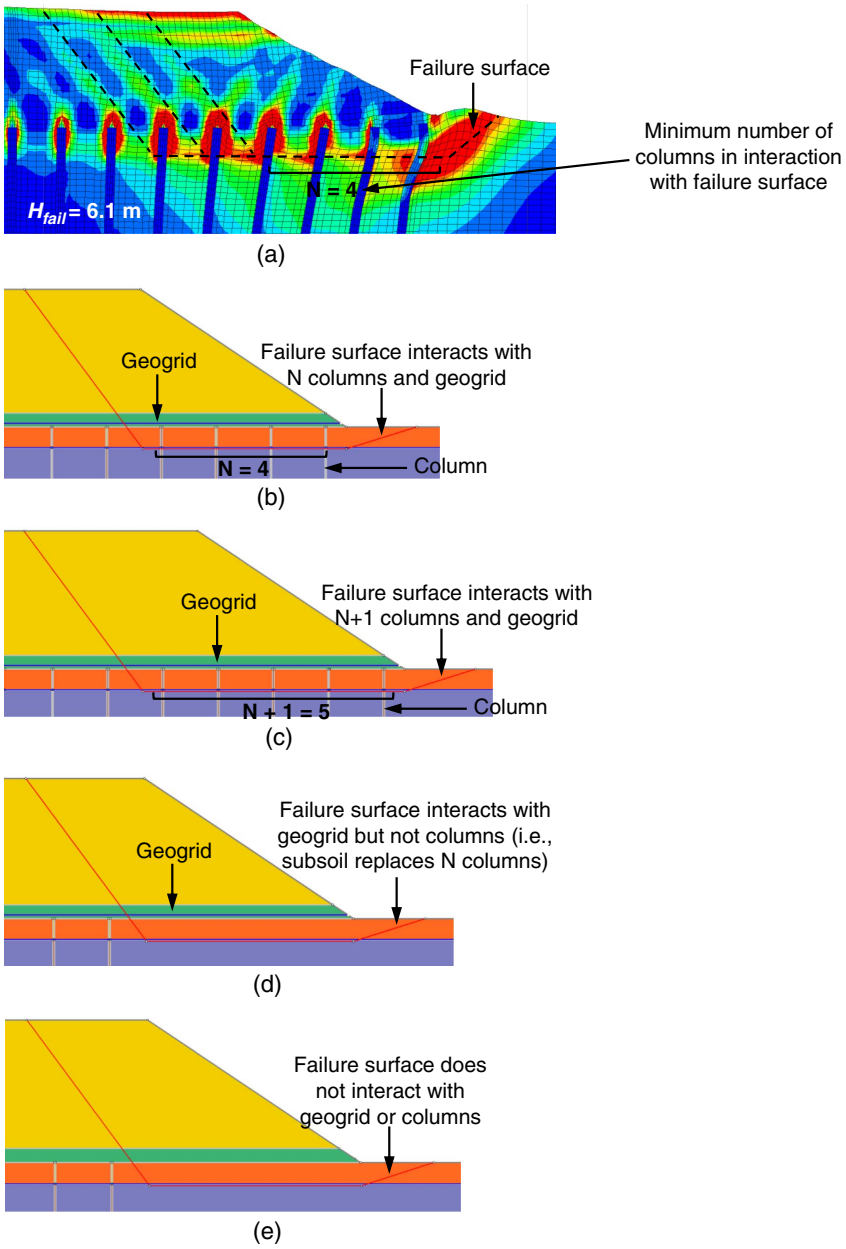

Fig. 9. Interaction of failure surface with columns and geogrid at the embankment failure height (using the base case as an example).

with the slip surface. Supporting evidence is provided by the FS for slip surfaces that interact with the geogrid but not any columns [Fig. 9(d)]: slip surface lengths are the same as those interacting with N columns [Fig. 9(b)], but the FS are much lower and closer to 1.0. Thus, it can be concluded from the combined analyses illustrated in Figs. 9(b–d) that the greater the number of concrete columns in interaction with the slip surface, the larger the FS. Unconservative FS were calculated because the LEM assumes failure by shear, whereas the unreinforced concrete columns failed not by shear but by bending and flexural tension.

- Comparing the two rightmost columns in Table 4, lower FS were calculated for the failure surfaces that did not interact with the geogrid than for the surfaces that did interact with the geogrid, and this was as expected. In addition, the removal of the geogrid resulted in unstable surfaces (FS $\leq$ 1.0) that were originally stable with the geogrid in place, and this corresponds to embankment failure occurring after geosynthetic tensile failure. Scenario 5 shows the largest decrease in the FS with geogrid removal, and this is because the geogrid has greater tensile strength. Results indicate that including geogrids in limit equilibrium stability analyses of CSEs can lead to calculations of higher than expected FS, especially for geogrids of greater tensile strengths.
- The LEM correctly calculated the FS ($\leq$1.0) when the failure surfaces were fully specified, and when both the geogrid and columns were removed. This is because failure indeed occurred on these particular surfaces in the soil, and the failure mechanism was by shear.

Implications for Design

The geosynthetic influenced both the ultimate and serviceability limit states, as determined by comparing the base case (J = 438 kN/m) with Scenario 3 (no geogrid) and Scenario 5 (J = 1,459 kN/m), which are scenarios that differ by only the geosynthetic. The geosynthetic influenced the ultimate limit state because

J. Geotech. Geoenviron. Eng., 2020, 146(12): 04020141

Table 4. Factors of safety for embankments at the failure height

Scenario	Circular failure surface (i.e., routine search for critical failure surface)[a]	Fully specified failure surface (i.e., same surface geometry as in 3D numerical analysis)			
		Failure surface interacts with N columns and geogrid [Fig. 9(b)]	Failure surface interacts with $N+1$ columns and geogrid [Fig. 9(c)]	Failure surface interacts with geogrid but not columns [Fig. 9(d)]	Failure surface does not interact with geogrid or columns [Fig. 9(e)]
Base case	1.19	4.88	5.52	1.12	0.95
1	1.31	4.64	5.57	1.23	1.00
2	1.18	3.61	3.96	1.10	0.96
3	1.20	5.27	6.05	Geogrid not included in original scenario	1.01
4	1.31	2.61	3.29	Geogrid not included in original scenario	1.04
5	1.16	4.31	4.67	1.18	0.84
6	1.15	3.5	3.71	FS not found	0.98
7	N/A	N/A	N/A	N/A	N/A

Note: Calculated using the 2D limit equilibrium Spencer's method of slices.
[a]Critical circular failure surfaces were all shallow failures within the embankment.

it influenced the failure height. Increasing the geosynthetic stiffness (and thus the tensile capacity) increased the failure height (H_{fail}), as shown in Table 1, by comparing the base case with Scenario 3 and by comparing Scenario 5 with the base case. The geosynthetic influenced the serviceability limit states by reducing lateral displacements and total settlements [Figs. 8(a–c)]. Using $J = 1{,}459$ kN/m (Scenario 5) was more effective in reducing deformations than using $J = 438$ kN/m (the base case).

The geosynthetic improved system ductility, as shown by the prefailure lateral toe displacements in Fig. 8(a). The prefailure lateral toe displacement is 0.56 m for the base case ($J = 438$ kN/m) and 0.32 m for Scenario 3 (no geogrid). All scenarios that included geosynthetic reinforcement calculated greater lateral displacements prior to failure than scenarios that did not include geosynthetic reinforcement, even for cases with the same failure height (Scenario 1 versus Scenario 3). These results indicate that the inclusion of geosynthetic in design can prevent sudden and catastrophic failures.

Comparisons of LEM and numerical analyses showed that the global stability of CSEs supported by unreinforced concrete columns should not be evaluated using the conventional LEM. Factors of safety were overstated because the actual failure mechanisms differ from the shear failures assumed in the LEM. Concrete columns did not fail in shear but in flexural tension at embankment heights much lower than produced collapse. The LEM assumes the geogrid's tensile resistance is fully mobilized at failure, whereas CSE failure initiated post geogrid tensile rupture, which means that the geogrid does not provide any resistance during failure. The only instance in which the LEM correctly calculated FS ≤ 1.0 for CSEs at failure height was when the failure surface geometry was known and fully specified and when both the geogrid and columns were excluded from the analysis. Unfortunately, the combination of these factors cannot be conveniently applied in practice: the failure surface geometry is typically an analysis output, and excluding structural elements from the stability analyses defeats their purpose of application, especially in CSEs. Outside of CSEs, application of the LEM is also inappropriate where geosystem failures are controlled by mechanisms other than shear.

Summary and Conclusions

The failure height, failure mode, and deformations of eight column-supported embankment scenarios were computed using the 3D finite difference method. The eight scenarios included a base case using typical concrete column design with an area replacement ratio of 2.8%, five single-parameter variations using base case conditions, and two cases with variations in multiple parameters that produced a significantly worse and better performance than the base case. Each CSE was incrementally increased in height in the undrained condition with excess pore water pressure development in the clay, followed by the dissipation of excess pore water pressures. Stability was evaluated at different heights, both at the undrained end-of-construction and the long-term dissipated conditions. Column properties represented unreinforced concrete, and a Mohr-Coulomb failure criterion was adopted to permit flexural tensile failure in the columns. The geosynthetic reinforcement was modeled using orthotropic linear elastic geogrid elements, whose tensile failure was manually implemented. The transverse geosynthetic strain was calculated for each unit cell bridging columns, and when the strain reached 10%, geogrid elements in the unit cell were removed.

The second part of the study was to investigate whether the conventional limit equilibrium method can be used to evaluate CSE global stability. Using a 2D LEM, factors of safety were calculated for the same embankment scenarios at failure height through a series of analyses that differed in the soil-structure interactions: (1) a typical circular surface search with the geogrid and columns included in the CSE models; (2) a fully specified failure surface whose geometry was derived from 3D numerical analyses and in interaction with the geogrid and columns; (3) a larger slip surface in interaction with one additional column compared to the slip surface in (2); (4) a same-sized slip surface as in (2) that was in interaction with the geogrid but not any of the columns; and (5) a same-sized slip surface as in (2) but with the geogrid and columns both excluded from the models.

Key findings are as follows:

- CSE stability was most critical at the undrained end-of-construction condition.
- Two CSE failure modes were found for the undrained condition: (1) Mode A involved multisurface shearing in the embankment, coupled with column bending failure and near-circular shear failure through the clay. Failure of columns initiated the closest to the embankment toe and retrogressed toward inner columns as the embankment height increased. As columns failed in bending, lateral displacements in the clay exceeded lateral displacements in the columns. (2) Mode B involved multisurface shearing in the embankment coupled with column bending failure and shearing within the top portion of the clay. The soil-column interactions

were complex, and the failure of columns retrogressed toward inner columns. With the increase in embankment height, columns near the embankment toe failed early in construction, followed by clay lateral displacements exceeding those of the columns and the degradation of inner columns with the increase in clay displacement.
- Where the geosynthetic was present, collapse in the undrained condition occurred after geosynthetic rupture.
- Geosynthetic rupture in the long-term dissipated condition did not lead to CSE failure.
- The geosynthetic contributed to both ultimate and serviceability limit states. It allowed the construction of taller embankments as well as reduced the lateral toe displacements and total settlements at the centerline.
- The geosynthetic increased the system's overall ductility and allowed for greater deformations before failure.
- Increasing the undrained shear strength of the clay by 9.6 kPa (200 psf) increased the embankment failure height by 6.1 m.
- The analyses indicate that a CSE could be constructed to a height of 12.8 m (42 ft) without failing for the following conditions: a center-to-center column spacing of 2.4 m (8 ft), a column diameter of 0.46 m (1.5 ft), a layer of geosynthetic with a stiffness of 1459 kN/m (100,000 lb/ft) and rupture at a 10% strain, and foundation conditions consisting of 0.9 m (3 ft) of existing loose fill overlying 15 m (50 ft) of soft clay with an undrained shear strength of 14.4 kPa (300 psf) at the top and increasing with depth at a rate of 1.7 kPa/m (11 psf/ft).
- The conventional limit equilibrium method (LEM) overstated the factor of safety when evaluating global stability of CSEs. This is because the LEM assumes failure by shear, whereas CSEs fail through a combined mechanism of shear in the soil, flexural tension in the unreinforced concrete columns, and tensile rupture in the geosynthetic. The LEM correctly calculated the FS only for fully specified failure surfaces whose geometries were inherited from numerical analysis and when the geogrid and columns were excluded from the analysis.

Alternative simplified approaches for CSE stability evaluation should be explored until 3D numerical analyses are used more routinely in practice.

Data Availability Statement

Some or all data, models, or code generated or used during the study are available from the corresponding author upon reasonable request.

Acknowledgments

This research was funded by the Center for Geotechnical Practice and Research at Virginia Tech. The anonymous reviewers provided valuable suggestions for additional analyses, broader discussions, and clarifications that significantly improved the paper. The authors appreciate the support and suggestions.

Notation

The following symbols are used in this paper:

a = edge length of square column cross-section;
c = cohesion;
c' = effective cohesion;
d = vertical deflection of geosynthetic reinforcement;
d_{col} = column diameter;
E = Young's modulus;
e_1 = void ratio at reference pressure;
f'_c = unconfined compressive strength;
f'_r = flexural tensile strength (modulus of rupture);
G = shear modulus;
H_{crit} = critical height;
H_{emb} = embankment height;
H_{fail} = embankment failure height;
J = geosynthetic stiffness (in longitudinal and transverse directions);
M = slope of critical state line;
N = minimum number of columns in interaction with failure surface;
p'_i = initial mean effective stress;
p'_o = preconsolidation pressure;
S_{col} = center-to-center column spacing;
s_u = undrained shear strength;
α = angle of shear failure surface from vertical;
Γ = specific volume at unit mean effective stress on critical state line;
γ = unit weight;
ΔS_{col} = change in center-to-center column spacing;
ε_{lat} = unit cell transverse strain in geogrid due to lateral spreading;
$\varepsilon_{\text{trans}}$ = unit cell transverse strain in geogrid;
$\varepsilon_{\text{vert}}$ = unit cell transverse strain in geogrid due to vertical deflection;
κ = slope of recompression line;
λ = slope of virgin compression line;
ν = Poisson's ratio;
σ = normal stress;
σ_t = tensile strength;
τ = shear stress;
υ_λ = specific volume at unit mean effective stress on normal compression line;
φ = friction angle; and
φ' = effective friction angle.

References

ACI (American Concrete Institute). 2011. *Building code requirements for structural concrete and commentary.* ACI 318-11. Farmington Hills, MI: ACI.

Adams, T. E. 2011. "Stability of levees and floodwalls supported by deep-mixed shear walls: Five case studies in the New Orleans area." Doctor of Philosophy, Dept. of Civil and Environmental Engineering, Virginia Polytechnic Institute and State Univ.

Ariyarathne, P., D. S. Liyanapathirana, and C. J. Leo. 2013. "Effect of geosynthetic creep on reinforced pile-supported embankment systems." *Geosynthetics Int.* 20 (6): 421–435. https://doi.org/10.1680/gein.13.00029.

BSI (British Standards Institution). 2010. *Design of embankments with reinforced soil foundations on poor ground*. BS 8006-1:2010. London: BSI.

BSI (British Standards Institution). 2016. *Design of embankments with reinforced soil foundations on poor ground*. BS 8006-1:2010+A1:2016. London: BSI.

Cancelli, A., P. Rimoldi, and S. Togni. 1992. "Frictional characteristics of geogrids by means of direct shear and pull-out tests." In *Proc., Int. Symp. on Earth Reinforcement Practice*, 29–34. Rotterdam, Netherlands: A.A. Balkema.

Cazzuffi, D., L. Picarelli, A. Ricciuti, and P. Rimoldi. 1993. "Laboratory investigations on the shear strength of geogrid reinforced soils." In *Geosynthetic soil reinforcement testing procedures*, 119–137. West Conshohocken, PA: ASTM.

Chai, J. C., S. Shrestha, T. Hino, and T. Uchikoshi. 2017. "Predicting bending failure of CDM columns under embankment loading." *Comput. Geotech.* 91 (Nov): 169–178. https://doi.org/10.1016/j.compgeo.2017.07.015.

Duncan, J. M., S. G. Wright, and T. L. Brandon. 2014. *Soil strength and slope stability*. Hoboken, NJ: Wiley.

Eun, J., R. Gupta, and J. G. Zornberg. 2017. *Effect of geogrid geometry on interface resistance in a pullout test*, 236–246. Orlando, FL: Geotechnical Frontiers.

Griffiths, D. V., and P. A. Lane. 1999. "Slope stability analysis by finite elements." *Géotechnique* 49 (3): 387–403. https://doi.org/10.1680/geot.1999.49.3.387.

Han, J., and M. A. Gabr. 2002. "Numerical analysis of geosynthetic-reinforced and pile-supported earth platforms over soft soil." *J. Geotech. Geoenviron. Eng.* 128 (1): 44–53. https://doi.org/10.1061/(ASCE)1090-0241(2002)128:1(44).

Huang, J., and J. Han. 2009. "3D coupled mechanical and hydraulic modeling of a geosynthetic-reinforced deep mixed column-supported embankment." *Geotext. Geomembr.* 27 (4): 272–280. https://doi.org/10.1016/j.geotexmem.2009.01.001.

Huang, Z. 2019. "Lateral spreading mechanics of column-supported embankments." Doctoral dissertation. Dept. of Civil and Environmental Engineering, Virginia Polytechnic Institute and State Univ.

Huang, Z., K. Ziotopoulou, and G. M. Filz. 2018. "Numerical predictions of deformations in geosynthetic-reinforced column-supported embankments: Validation of manual dissipation of excess pore pressure approach for undrained and drained analyses." In *Proc., IFCEE 2018: Innovations in Ground Improvement for Soils, Pavements, and Subgrades, GSP*, 327–336. Reston, VA: ASCE. https://doi.org/10.1061/9780784481592.033.

Huang, Z., K. Ziotopoulou, and G. M. Filz. 2019. "3D numerical limiting case analyses of lateral spreading in a column-supported embankment." *J. Geotech. Geoenviron. Eng.* 145 (11): 04019096. https://doi.org/10.1061/(ASCE)GT.1943-5606.0002162.

Huesker. 2019. "Product overview." Accessed October 8, 2019. https://www.huesker.us/fileadmin/Media/Brochures/US/Product_Overview_Geosynthetics_GB.pdf.

Inagaki, M., M. Yamamoto, M. Nozu, Y. Yanagawa, and L. Li. 2012. "Behavior of cement deep mixing columns under road embankment." In *Proc., Physical Modeling in Geotechnics: ICPMG'02*, 967–972. Rotterdam, Netherlands: A.A. Balkema.

INOVA Geosynthetics. 2017. "Geoter® F range high strength reinforcement geocomposites." Accessed October 8, 2019. http://www.inova-geo.com/high-strength-reinforcement.html.

Itasca. 2013a. *FLAC3D theory and background*. Minneapolis: Itasca.

Itasca. 2013b. *Structural elements*. Minneapolis: Itasca.

Jamsawang, P., P. Voottipruex, P. Boathong, W. Mairaing, and S. Horpibulsuk. 2015. "Three-dimensional numerical investigation on lateral movement and factor of safety of slopes stabilized with deep cement mixing column rows." *Eng. Geol.* 188 (Apr): 159–167. https://doi.org/10.1016/j.enggeo.2015.01.017.

Jenck, O., D. Dias, and R. Kastner. 2009. "Three-dimensional numerical modeling of a piled embankment." *Int. J. Geomech.* 9 (3): 102–112. https://doi.org/10.1061/(ASCE)1532-3641(2009)9:3(102).

King, J. D., A. Bouazza, J. R. Gniel, R. K. Rowe, and H. H. Bui. 2018. "Geosynthetic reinforced column supported embankments and the role of ground improvement installation effects." *Can. Geotech. J.* 55 (6): 792–809. https://doi.org/10.1139/cgj-2017-0036.

Kitazume, M., and K. Maruyama. 2007. "Centrifuge model tests on deep mixing column failure under embankment loading." In *Advances in deep foundations*, 379–383. London: Taylor & Francis.

Liao, X., G. Ye, and C. Xu. 2009. "Friction and passive resistance of geogrid in pullout tests." In *Advances in ground improvement: Research to practice in the United States and China*, 252–259. Reston, VA: ASCE. https://doi.org/10.1061/41025(338)27.

Liu, C., Y. Ho, and J. Huang. 2009. "Large scale direct shear tests of soil/PET-yarn geogrid interfaces." *Geotext. Geomembr.* 27 (1): 19–30. https://doi.org/10.1016/j.geotexmem.2008.03.002.

Mahdavi, H., B. Fatahi, H. Khabbaz, P. Vincent, and R. Kelly. 2016. "Comparison of coupled flow-deformation and drained analyses for road embankments on CMC improved ground." *Procedia Eng.* 143 (Jan): 462–469. https://doi.org/10.1016/j.proeng.2016.06.058.

McGuire, M. P. 2011. "Critical height and surface deformation of column-supported embankments." Doctoral dissertation, Dept. of Civil and Environmental Engineering, Virginia Polytechnic Institute and State Univ.

Navin, M. P. 2005. "Stability of embankments founded on soft soil improved with deep-mixing-method columns." Doctor of Philosophy, Dept. of Civil and Environmental Engineering, Virginia Polytechnic Institute and State Univ.

Plomteux, C., and M. Lacazedieu. 2007. "Embankment construction on extremely soft soils using controlled modulus columns for Highway 2000 project in Jamaica." In *Proc., 16th Southeast Asian Geotechnical Conf.*, edited by K. Yee, O. T. Aun, T. W. Hui, and C. S. Fatt, 533–539. Thailand: Southeast Asian Geotechnical Society.

Potyondy, J. G. 1961. "Skin friction between various soils and construction materials." *Géotechnique* 11 (4): 339–353. https://doi.org/10.1680/geot.1961.11.4.339.

Pul, S., A. Ghaffari, E. Öztekin, M. Hüsem, and S. Demir. 2017. "Experimental determination of cohesion and internal friction angle on conventional concretes." *ACI Mater. J.* 114 (3): 407–416. https://doi.org/10.14359/51689676.

Santacruz Reyes, K. J. 2016. "Geosynthetic reinforced soil: Numerical and mathematical analysis of laboratory triaxial compression tests." Ph.D. dissertation, Dept. of Civil and Environmental Engineering, Virginia Polytechnic Institute and State Univ.

Schädlich, B., and H. Schweiger. 2014. *Internal report shotcrete model: Implementation validation and application of the shotcrete model*. Delft, Netherland: Plaxis.

Schaefer, V. R., R. R. Berg, J. G. Collin, B. R. Christopher, J. A. DiMaggio, G. M. Filz, D. A. Bruce, and D. Ayala. 2017. *Ground modification methods reference manual—Volume II*. Washington, DC: Federal Highway Administration.

Shrestha, S., J. C. Chai, D. T. Bergado, T. Hino, and Y. Kamo. 2015. "3D FEM investigation on bending failure mechanism of column inclusion under embankment load." *Lowland Technol. Int.* 17 (3): 157–166. https://doi.org/10.14247/lti.17.3_157.

SHRP2 (Strategic Highway Research Program 2). 2012. "Column-supported embankments." Accessed October 4, 2018. http://www.GeoTechTools.org.

Sloan, J. A. 2011. "Column-supported embankments: Full-scale tests and design recommendations." Doctoral dissertation, Dept. of Civil and Environmental Engineering, Virginia Tech.

Sloan, J. A., G. M. Filz, J. G. Collin, and P. Kumar. 2014. *Column-supported embankments: Field tests and design recommendations*. 2nd ed. Blacksburg, VA: Virginia Tech Center for Geotechnical Practice and Research.

Tensar International Corporation. 2015. "Product specification Tensar biaxial geogrid." Accessed October 8, 2019. https://www.tensarcorp.com/Systems-and-Products/Tensar-Biaxial-BX-geogrids.

Wood, D. M. 1990. *Soil behavior and critical state soil mechanics*. Cambridge, UK: Cambridge University Press.

Yapage, N. N. S., D. S. Liyanapathirana, H. G. Poulos, R. B. Kelly, and C. J. Leo. 2013. "Analytical solutions to evaluate bending failure of column supported embankments." *Int. J. Eng. Technol.* 5 (4): 502–507. https://doi.org/10.7763/IJET.2013.V5.606.

Zanzinger, H., and E. Gartung. 2002. "Performance of a geogrid reinforced railway embankment on piles." In *Proc., 7th ICG*, 381–386. Rotterdam, Netherlands: A.A. Balkema.

Zhang, C., G. Jiang, X. Liu, and O. Buzzi. 2016. "Arching in geogrid-reinforced pile-supported embankments over silty clay of medium compressibility: Field data and analytical solution." *Comput. Geotech.* 77: 11–25. https://doi.org/10.1016/j.compgeo.2016.03.007.

Zhang, J. S., C. Guo, and S. W. Xiao. 2012. "Analysis of effect of CFG pile composite foundation pile spacing on embankment stability based on centrifugal model tests." *Appl. Mech. Mater.* 178: 1641–1648. https://doi.org/10.4028/www.scientific.net/AMM.178-181.1641.

Zhang, Z., J. Han, and G. Ye. 2014. "Numerical analysis of failure modes of deep mixed column-supported embankments on soft soils." *Ground Improv. Geosynthetics* 238: 78–87. https://doi.org/10.1061/9780784413401.008.

Zhuang, Y., and K. Y. Wang. 2015. "Three-dimensional behavior of biaxial geogrid in a piled embankment: Numerical investigation." *Can. Geotech. J.* 52 (10): 1629–1635. https://doi.org/10.1139/cgj-2014-0538.